In: EUSAR 2022: 14th European Conference on Synthetic Aperture Radar, Leipzig, 25-27 July 2022
https://ieeexplore.ieee.org/document/9944245

Multistatic 3D SAR Imaging with Coarse Elevation and Azimuth Sampling

Richard Welsh*[a], Daniel Andre[a], Mark Finnis[b]
[a] Centre for Electronic Warfare Information and Cyber, Cranfield University, Defence Academy of the United Kingdom, Shrivenham, UK
[b] Centre for Defence Engineering, Cranfield University, Defence Academy of the United Kingdom, Shrivenham, UK
contact email: Richard.welsh@cranfield.ac.uk

Abstract

It is advantageous to produce Synthetic Aperture Radar (SAR) renderings in three dimensions as these allow the separation of features in height, providing additional target information. A Nyquist sampled 2D SAR aperture produces high quality 3D imagery, however the large scanning time and data storage requirements make this method impractical for use in many scenarios. This paper investigates the formation of 3D target renderings from sparsely sampled 2D aperture Multistatic SAR geometries. The investigation employed both simulations and measured multistatic data collected at the Ground Based SAR (GBSAR) Laboratory at Cranfield University.

1 Introduction

The optimisation of the 3D Volumetric Synthetic Aperture Radar (SAR) Imaging process presents an opportunity for generating detailed three-dimensional renderings of a target structure, fully utilising the advantages that a SAR system brings. SAR systems use the horizontal trajectory of an antenna to cover a wider area and generate images of a smaller azimuth spatial resolution than would be possible for a stationary antenna of the same size [1]. Producing SAR renderings in 3D has the main advantages of the separation of target features in the vertical direction, and the removal of overlay artefacts for elevated scatteres. However, producing high quality 3D SAR renderings typically requires a finely sampled 2D aperture window where the radar data is collected over a wide range of elevation and azimuth angles, with spacing between positions corresponding to that required for Nyquist sampling. This collection geometry requires many passes of the target scene by a radar antenna and would be impractical to conduct in many scenarios due to the large data collection time and cost involved [2], [3].

There has been considerable research effort conducted in the generation of 3D SAR renderings from coarsely collected samples, with varoius studies investigating novel radar trajectories as a method of obtaining a higher vertical resolution than would be possible for a sparse linear collection. This includes the utilisation of a sinusoidal and circular trajectories, which have been found to spread aliasing artefacts and to reduce clutter in 3D SAR renderings, compared to that of a straight line sampled sparse data set [4], [5].

Multistatic antenna geometries are investigated in this study as they allow for the backscattered radiation to be measured at multiple different collection angles simultaneously, thus increasing the spatial sampling without a subsequent increase in the data collection time [6], [7]. This study will look at two approaches for improving the quality of 3D SAR imagery from data sets sampled coarsely in elevation:

1. A multistatic approach – although the transmitter may sweep coarse sampling in elevation, by use of several receivers distributed in height, an effective Nyquist sampling can be achieved. This approach is implemented with a conventional SAR image formation algorithm [8].
2. An approach based on a novel interferometry-based 3D image formation algorithm, designed to cope with overall coarse sampling of trajectories distributed in height.

The investigations for the first part of this study primarily use multistatic measurements conducted using the equipment of the GBSAR laboratory, whilst the second part uses both simulations and experimental measurements of a laboratory scene for investigating the novel image formation algorithm.

2 SAR Point Cloud Generation System

The second part of this study implements and extends the patented SAR Point Cloud Generation System (SPCGS) [9]. The SPCGS requires a target scene to be scanned from N different phase centre heights, producing N complex SAR images via conventional 2D image formation algorithms, such as the Back Projection Algorithm (BPA). The first of the N complex 2D SAR images is used as a reference image in order to form an interferogram with the remaining secondary N-1 complex SAR images. The 'secondary images' are geometrically co-registered to the reference to account for differences in layover position of elevated scatterers.

The measured phase differences, for each interferogram, are combined to produce a measured interferometric response function (MIRF) at each pixel position,

$$\boldsymbol{MIRF(h)} = \frac{1}{N-1}\left|1 + \sum_{n=1}^{N-1} e^{(\varphi_{n,meas} - i\beta_n h)}\right| \quad (1)$$

$\varphi_{n,meas}$ is the phase of the n^{th} interferogram, β_n is the interferometric scale factor of the interferogram based on known geometry and h is the height estimate of a scatterer. The SPCGS method calculates the MIRF values over a large range of scatterer height estimates, with the estimates producing a MIRF value above a certain threshold being used as the height of a scatterer situated at a certain pixel position. The scatterer height estimates are then stored at each pixel position, as well as the average intensity for each pixel of the N complex SAR images.

This paper implements the co-registration for the complex SAR images by setting a SAR BPA focal surface to the height estimates of the scatterers. The effect of this is that there will be no difference in layover between the N complex 2D SAR images when the focal surface is at the correct height of a scatterer; the height of the focal surface is then used in the interferometric sum calculations, with the focal surface producing the peak MIRF values being the one used as the height of a scatterer. Furthermore, this paper additionally weights the interferometric contribution of each interferogram against the pixel brightness in the corresponding complex SAR image; this means that the scatterers in the scene contribute to the interferometric sum much more than artefacts in the image thus improving resolution. The extended SPCGS algorithm, developed and used in this study, is represented by the flow chart in Figure 1.

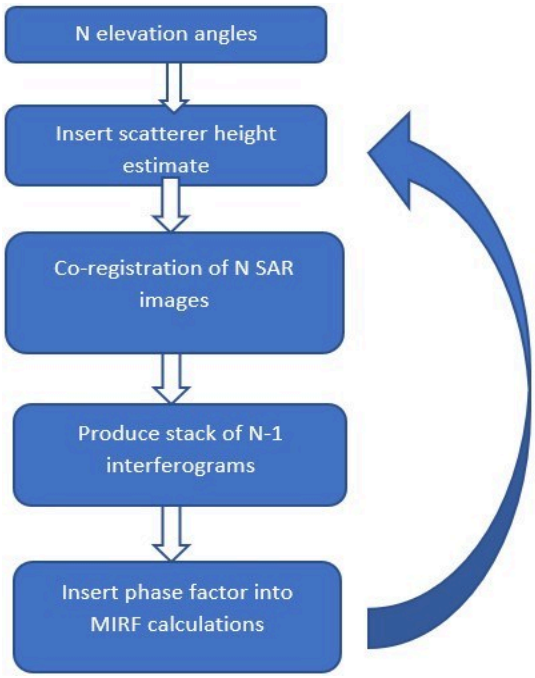

Figure 1: Algorithm flow chart showing SPCGS steps.

The algorithm developed here is considered an extension of the original SPCGS, as it implements pixel intensity weighting in the interferometric summation and is applicable to SAR near-field scenarios and bistatic geometries, so that its applicability is more general.
The study aims to determine the potential of the extended SPCGS in determining accurate height estimates of simple scatterers, from coarsely sampled SAR collection geometries.

3 Laboratory Measurements

3.1 Tank Scene Measurement

The Multistatic SAR aperture data was generated using the Cranfield University Ground Based SAR system. This system is based on the operation of a Vector Network Analyser (VNA), connected to receiver and a transmitter Ultra-Wideband horn antenna. These are separately moved on respective two-dimensional scanners, in vertical planes. The accurate nature of transceiver trajectory positions allows for high quality images to be produced, which aids the development novel radar modes and image formation algorithms. Figure 2 shows the transceiver trajectories used in the laboratory, while Figure 3 shows the first scene that was scanned by the GBSAR system. The setup can be used to generate both finely sampled and coarsely sampled 2D aperture data with a horizontal width of 3.5 m and a change in height of 1.5 m for both monostatic and bistatic geometries.

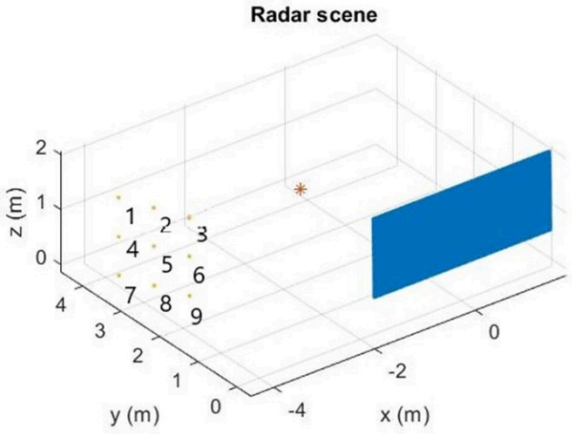

Figure 2: Diagram of multistatic radar geometry, with dense 2D transmitter aperture in red and nine reciever positions numbered. Scene centre indicated by red asterisk.

Figure 3: Photograph of the model tank target scene, pictured from behind the transmitter axis.

For the first part of this study, a multistatic data set has been collected of a quarter-scale T-72 tank model situated on a gravel scene. The target scene consists of a gravel area, roughly of the dimensions 2.0 x 2.5m, onto which a metal coated quarter scale model of the tank was placed, with the cannon facing the transmitter axis, as seen in Figure 3. The measurement had a 15 mm spacing between transmitter positions in the horizontal and vertical directions; individual transmitter heights can be extracted from the 2D aperture, providing a down-sampled to investigate image formation with a coarsely sampled target scene. The receiver positions form a rectangular grid, coarse in azimuth and elevation, with spacings of 725 mm and 642.5 mm in the vertical and horizontal directions respectively. In addition to the multistatic collection, a quasi-monostatic data set was also obtained by placing a receiver on the same aperture as the transmitter, with a 255 mm offset, using a 10 mm spacing between pulse positions in the vertical and horizontal directions. All four polarisation channels were measured: VV, VH, HV and HH, conducted in separate scans to extract more information from the target scene. The frequency range used for this part of the study was 6.62-10 GHz.

3.2 Sphere Scatterer Scene

Monostatic laboratory measurements were conducted on a scene of sphere scatterers, with the sphere centres placed at the same location as the point scatterers in the simulations. The scan was conducted using a frequency range of 6.62-10 GHz, with a 10 mm spacing in the vertical and horizontal directions, and aperture width of 1450 mm in the horizontal and vertical directions, for all four polarisation channels. The scanned target scene is shown in Figure 4.

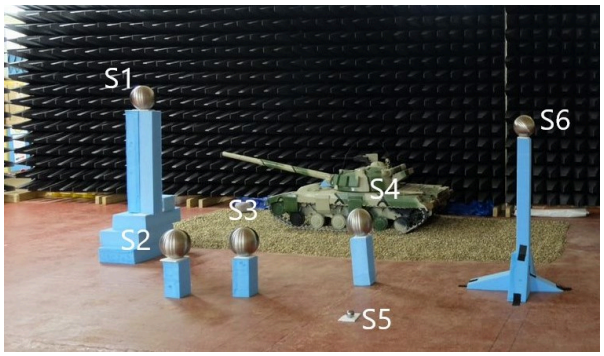

Figure 4: Photograph of scene of sphere scatterers.

4 Results

4.1 Tank Scene Measurements

4.1.1 Fully Nyquist Sampled

To form high quality initial imagery for comparison, the first 3D SAR rendering formed from the collected data set employed a monostatic transceiver arrangement, with a finely sampled collection geometry that spanned the full width and height of the 2D SAR aperture described in the Laboratory Measurements section. This formed high quality maximum intensity projections of the laboratory scene, shown in Figure 5 in the VV polarisation channel, where the features of the tank are shown to be clearly separated in the vertical direction.

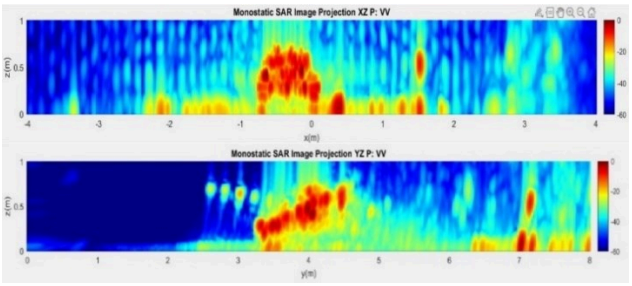

Figure 5: Monostatic maximum intensity projections of the measured model tank scene, for XZ and YZ planes, collected at the Nyquist sampling rate.

The top image in Figure 5 is a maximum intensity projection in the XZ plane. The front cross section of the tank structure, which is characterised by the area of high brightness in the centre of the image. The elevated large sphere at the back of the tank scene, is shown to the right of the tank structure at a cross-range of 1.52 m, and a height of 0.52 m.

The bottom image in Figure 5 is a maximum intensity projection in the YZ plane, showing the length and height of the tank structure. The main tank structure is situated centrally in the projection shown, with the cannon of the tank shown extending outwards from the front of the main tank structure. The SAR renderings shown in Figure 5 represent high qualtiy 3D SAR renderings, using typical image formation methods, and will allow a comparison with multistatic renderings presented in the next section (Figure 6 and Figure 7).

4.1.2 Coarse Multistatic Geometry

The tank model volumetric SAR projected images shown in Figure 6 and Figure 7 were produced using a downsampled collection geometry, from a multistatic collection geometry shown in Figure 2. The downsampled collection geometry consisted of only six transmitter heights and nine stationary receiver positions, shown in Figure 8. In this figure, the equivalent monostatic positions – the collection of points half-way between the receiver and transmitter – are shown in green.

The images in Figure 6 were formed by downsampling the data set from a finely-sampled wide transmitter aperture to a coarsely-sampled wide transmitter aperture. The maximum intensity projections presented were formed from a non-coherent sum of the nine datasets corresponding to the nine receiver positions. The features of the tank structure shown in the projections are noticeably coarse in appearence, which shows deterioration in the vertical resolution expected when the vertical aperture width is downsampled.

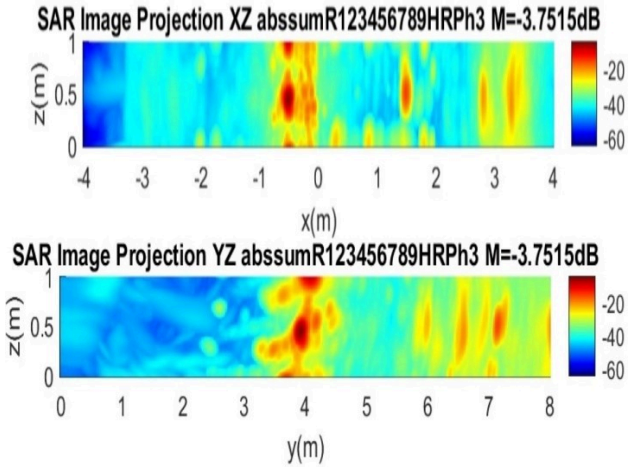

Figure 6: Mulstistatic Volumetric SAR projections of a non-coherent sum of the nine datasets corresponding to each of the nine reciever positions, and with a coarsely sampled vertical transmitter aperture.

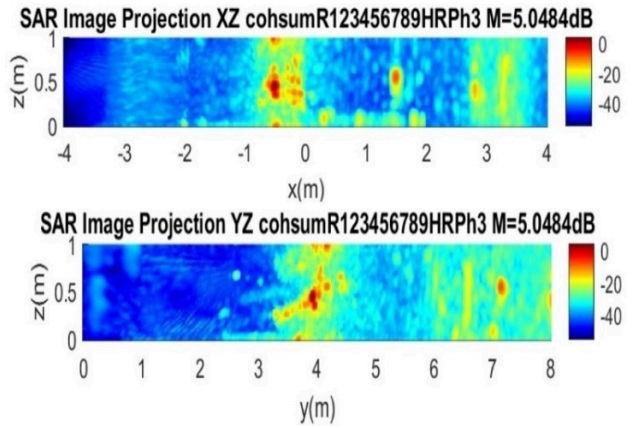

Figure 7: Mulstistatic Volumetric SAR projections of coherent sum of the nine datasets corresponding to each of the nine reciever positions, and with a coarsely sampled vertical transmitter aperture.

The volumetric SAR projections shown in Figure 7 show an improved 3D imaging performance of the coarsely sampled SAR geometries, when using the multistatic antenna arrangement. These SAR images were formed from a coherent summation of the nine datasets corresponding to the nine receiver positions. Performing a coherent summation allows for the combination of phase information from the nine receiver positions, which means that the effective vertical aperture width is improved without increasing the number of transmitter heights used. The effects of this are shown by the refinement of the features of the tank structure shown in Figure 7, compared to those presented in Figure 6, showing that adding the multiple receiver heights improves the vertical resolution. It is also likely that the unambiguous vertical cross-range extend would increase, though it is difficult to ascertain this in these results. The collection geometry used to produce both Figure 6 and Figure 7 is shown in Figure 8.

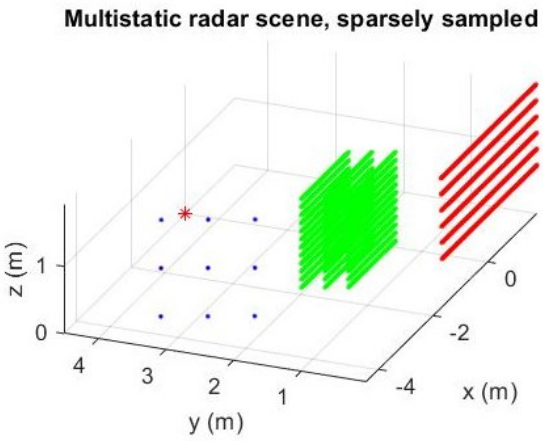

Figure 8: Downsampled Radar collection geometry, with nine stationary reciever positions, shown in blue, and five transmitter heights shown in red. The equivalent monostatic positions are shown in green.

The effect of the multistatic geometry on the unambiguous vertical cross-range extent is demonstrated by comparison with the monostatic volumetric SAR projection shown in Figure 9, produced using the same coarse transmitter aperture and where the receiver follows the transmitter motion.

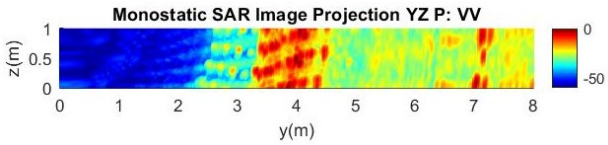

Figure 9: Coarse monostatic geomtery volumetric SAR projection in the YZ plane, showing significant aliasing in the vertical direction.

Multiple vertical repetitions of the tank structure can be seen in Figure 9, which is an aliasing effect due to a short unambiguous vertical cross-range extent. This is due to insufficient sampling in the vertical dimension for the target height. Comparing this result with Figure 7, the separation of aliasing artefacts is significantly greater than in Figure 9 indicating that the addition of multiple receivers at different heights resulted in a noticeable improvement in image quality.

4.2 Extended SPCGS Algorithm

4.2.1 Simulated Data

In order to determine the performance of the extended SPCGS image formation algorithm, simulations were first carried out on a simulated target scene of point scatterers, placed at the location of the spheres shown in Figure 4. The antenna geometry used in the simulations is described in section 3.2.

From the simulated antenna geometry, 7 random transceiver pass heights were extracted from the full set, and used to generate the phase history data for the point scatterer scene. The simulated phase history data was then input to the extended SPCGS (Figure 1). The 2D SAR images, used to provide the phase information for the extended SPCGS, were formed using the BPA. Figure 10

is a rendering produced from the 3D target information of the point scatterer scene, produced by the extended SPCGS, and Figure 11 shows the geometry used. The blue points in the figure are point cloud detections for the scatterers, and underlying these is the actual scatterer position marked with a red asterisk.

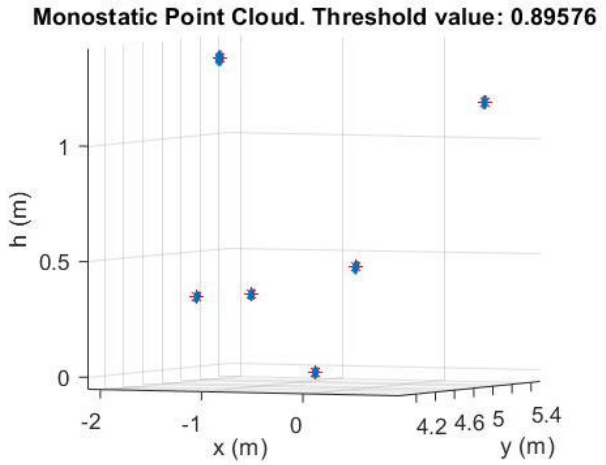

Figure 10: SAR point cloud rendering formed from simulated point scatterer scene data. Blue point clouds indicate algorithm detections, and scatterer actual positions are marked by partly obscured red asterisks.

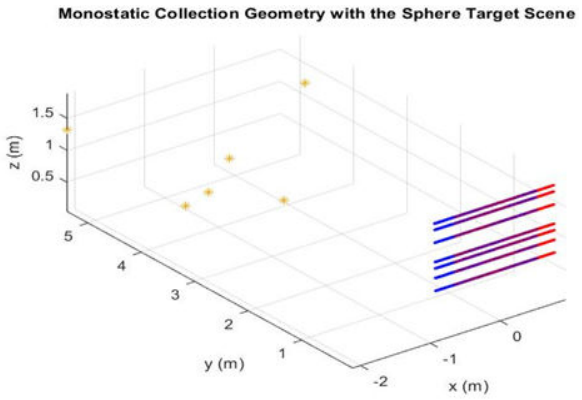

Figure 11: Pseudo monostatic collection geometry used to form SAR point cloud renderings on simulated data and data collected from the laboratory. Transmitter positions are in red, and receiver positions in blue.

In the application of the extended SPCGS algorithm, 141 separate scatterer height estimates, between the values of 0 and 1.41 m, were used to obtain the interferometric values required for generating the 3D SAR point cloud rendering. The spread of each point cloud in height, for each individual simulated point scatterer, is given in Table 1.

The finest resolution obtained from the extended SPCGS simulation was that of sphere 5, for which a resolution of 30 mm was produced from a collection geometry of 7 individual transceiver passes, over an aperture height of 0.7 m and an average vertical spacing of 103 mm; the same collection geometry using the BPA would be expected to achive an 117mm vertical resolution. Furtheremore, the vertical unambiguous cross-range for the same geometry would be 0.82 m using the BPA, which would be insufficient to cover the vertical extent of the scatterer scene.

Table 1: Vertical spread of SPCGS point clouds, compared to the true height of each scatterer. Δh is the spread of each scatterer point cloud in the vertical direction.

Sphere Index	Measured Height/cm	Δh/cm
1	132.2	5
2	34.8	3
3	35.5	3
4	46.5	4
5	3.9	3
6	118.1	4

4.2.2 Laboratory Data

The main aim of the laboratory measurements on the sphere scatterer scene was to investigate the algorithm when applied to real data, where variables such as the antenna beam pattern, non-zero scatterer dimensions, and varying scatterer brightness would be present. The 3D SAR point cloud rendering presented in Figure 12 was produced using the phase history data collected for the scan of the sphere scatterer scene, outlined in section 3.2. The downsampled collection geometry used to produce the simulations were also used to produce the SAR point cloud renderings from real laboratory data.

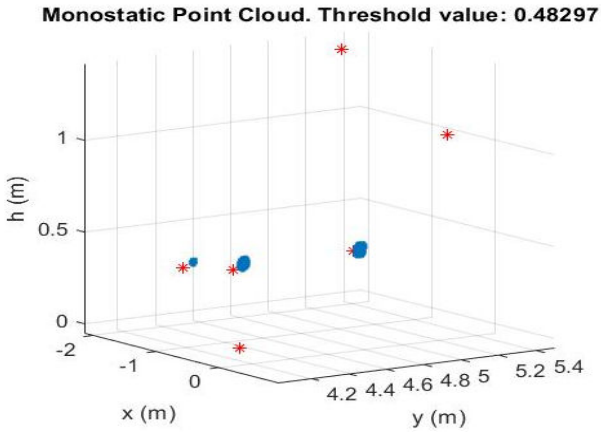

Figure 12: SAR Point Cloud rendering formed from data collected in the laboratory. Blue point clouds indicate the algorithm detections, and scatter ground truth positions are marked by red asterisks.

In Figure 12, point clouds form in proximity to the known sphere locations, for spheres 2, 3 and 4 pictured in Figure 4. The point cloud was extracted using a threshold 0.5 times the maximum weighted interferometric response value. Reducing the threshold further introduces a considerable amount of artefacts. Spheres 2, 3 and 4 are situated within a central position within the radar scene, and are the brightest scatterers within the scene. The relative brightness of the different scatterers within the scene is shown in Figure 13, which is a maximum intensity

projection formed using the BPA applied to the Nyquist sampled collection aperture of the sphere dataset. Multipath artefacts of a significant brightness are situated in the centre of the projection, showing a similar brightness to the spheres 1, 5 and 6.1

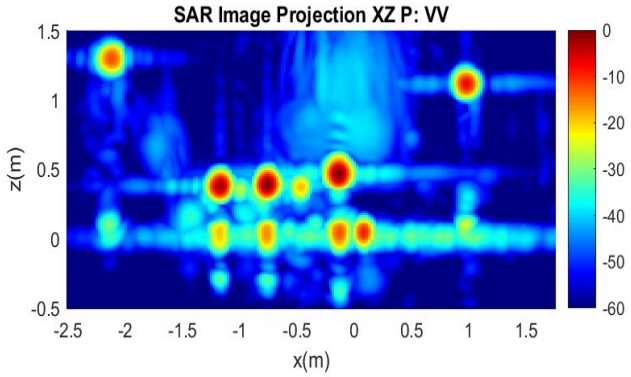

Figure 13: BPA image of the scene of sphere scatterers. Projection in the XZ plane.

5 Conclusions

The results for the investigation into the use of multistatic SAR geometries with coarsely sampled 2D collection apertures, showed that adding multiple receiver heights provided sufficient resolution and coverage for imaging the main structure of the model quarter scale tank, and an improvement over the monostatic geometry. Having shown this, a more deterministic relationship between the effective vertical sampling of the multistatic arrangement and the 3D imaging performance now needs to be determined, this would be essential for the practical implementation of real-life scenario multistatic SAR geometries.

Investigation into the developed extended SPCGS showed that the algorithm is effective at producing high resolution 3D SAR renderings of individual point scatterers. However, the performance of the algorithm needs to be improved for real data images which have varying scatterer brightness and background artefacts. Using variable detection thresholds across the image could potentially solve this. The investigation of the extended SPCGS algorithm into more complex target scenes with antenna bistatic and multistatic geometries is ongoing.

6 Literature

[1] C. Jakowatz Jr, D. Wahl, P. Eichel, D. Ghiglia, and P. Thompson, *Spotlight-Mode Synthetic Aperture Radar: A Signal Processing Approach*. Boston: Kluwer Academic Publishers, 1996.

[2] C. D. Austin, E. Ertin, and R. L. Moses, "Sparse signal methods for 3-D radar imaging," *IEEE Journal on Selected Topics in Signal Processing*, vol. 5, no. 3, pp. 408–423, Jun. 2011, doi: 10.1109/JSTSP.2010.2090128.

[3] A. Budillon, A. Evangelista, and G. Schirinzi, "SAR tomography from sparse samples," in *International Geoscience and Remote Sensing Symposium (IGARSS)*, 2009, vol. 4. doi: 10.1109/IGARSS.2009.5417514.

[4] D. André, "An analysis of 3D SAR from single pass nonlinear radar platform trajectories," in *Algorithms for Synthetic Aperture Radar Imagery XVII*, Apr. 2010, vol. 7699, p. 769908. doi: 10.1117/12.850093.

[5] L. Moore, L. Potter, and J. Ash, "Three-dimensional position accuracy in circular synthetic aperture radar," *IEEE Aerospace and Electronic Systems Magazine*, vol. 29, no. 1, pp. 29–40, 2014, doi: 10.1109/MAES.2014.130076.

[6] G. Krieger, N. Gebert, and A. Moreira, "Unambiguous SAR signal reconstruction from nonuniform displaced phase center sampling," *IEEE Geoscience and Remote Sensing Letters*, vol. 1, no. 4, pp. 260–264, Oct. 2004, doi: 10.1109/LGRS.2004.832700.

[7] C. Chung, S. Kim, J. Kim, U. Lee, B. Lee, and M. H. Ka, "Analysis on the Impact of Constellation Configuration over Multistatic SAR Images," 2021. doi: 10.1109/APSAR52370.2021.9688406.

[8] L. A. Gorham and L. J. Moore, "SAR image formation toolbox for MATLAB," in *Algorithms for Synthetic Aperture Radar Imagery XVII*, Apr. 2010, vol. 7699, p. 769906. doi: 10.1117/12.855375.

[9] R. Carande and D. Cohen, "SAR Point Cloud Generation System," WO/2014/074631, 2014